Journal of Cluster Science (2025) 36:196
https://doi.org/10.1007/s10876-025-02908-w

ORIGINAL PAPER

Structures and Bonding of Lanthanide-Doped Endohedral Borospherenes Ln@B$_{40}$$^{0/+}$ (Ln = Ce, Pr, Nd, Pm, Sm, Eu, Gd)

Xiao-Ni Zhao[1] · Ting Zhang[1] · Xiao-Qin Lu[2] · Si-Dian Li[1]

Received: 12 April 2025 / Accepted: 16 August 2025

Abstract

Metal-doped endohedral borospherenes M@B$_{40}$ have attracted considerable attention since the discovery of the first boroshphenes B$_{40}$$^{-/0}$ in 2014. Systematical density functional theory investigations performed herein unveil the ground-state structures and coordination bonding patterns of a series of lanthanide-doped endohedral borospherenes Ln@B$_{40}$$^{0/+}$, including the doublet C_{2v} Ce@B$_{40}$$^{+}$ (**1**, ^{2}B$_1$), triplet C_{2v} Ce@B$_{40}$ (**2**, ^{3}A$_2$), quartet C_{2v} Pr@B$_{40}$ (**3**, ^{4}B$_1$), quintet C_{2v} Nd@B$_{40}$ (**4**, ^{5}A$_1$), sextet C_2 Pm@B$_{40}$ (**5**, ^{6}A), septet C_{2v} Sm@B$_{40}$ (**6**, ^{7}A$_2$), octet D_{2d} Eu@B$_{40}$ (**7**, ^{8}B$_1$), and octet C_{2v} Gd@B$_{40}$$^{+}$ (**8**, ^{8}A$_2$). Detailed principal interaction spin orbital (PISO) and adaptive natural density partitioning (AdNDP) bonding pattern analyses indicate that, with the number of unpaired α-electrons changing from n_α = 1, 2, 3, 4, 5, 6, 7, to 7 in the series, their coordination bonding energies decrease monotonically from E_c = 7.22, 6.93, 5.67, 4.85, 4.67, 4.29, 4.02, to 2.07 eV, respectively, with the dominating percentage contributions of the Ln 5d-involved PISOs to the overall E_c increasing almost monotonically from 66 to 83%, while the minor contributions of the Ln 4f-involved PISOs varying between 0.3% and 12.1% and that of Ln 6s-involved PISO pairs remaining basically unchanged in a narrow range between 6% and 8%. In average, the dominating 5d-invloved PISOs in Ln@B$_{40}$ contribute about 72.8% to the overall E_c, 19.3% higher than that (53.4%) of the 6d-involved PISOs in the newly reported actinide-doped An@B$_{40}$$^{+/0/-}$, while the minor 4f-involved PISOs in Ln@B$_{40}$ contribute about 6.1% to E_c, 15.7% lower than that (21.8%) of the 5f-invloved PISOs in An@B$_{40}$$^{+/0/-}$, quantitatively unveiling the differences in coordination bonding patterns between Ln@B$_{40}$$^{+/0}$ and An@B$_{40}$$^{+/0/-}$.

Graphical Abstract

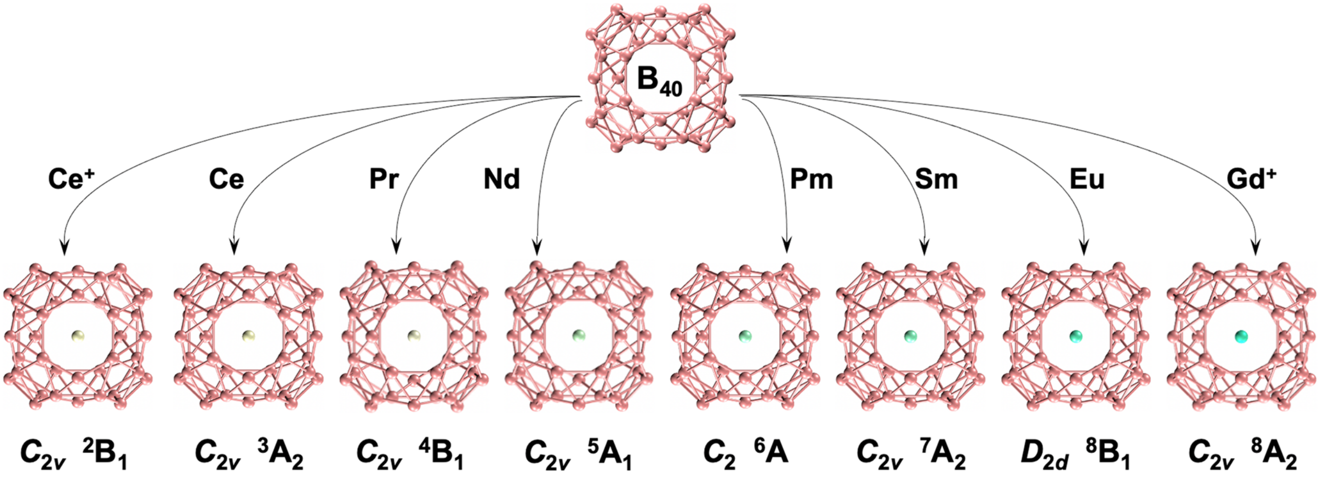

Keywords Lanthanides · Metallo-Borospherenes · First-Principles theory · Structures · Coordination bonding patterns

---

Extended author information available on the last page of the article

Introduction

The discovery of the first all-boron fullerenes D2d B40-/0 in 2014 [1] and C3/C2 B39- in 2015 [2] marks the onset of borospherene chemistry. In the past one decade, the study of metal-doped B40 has involved integrating main group and transition metals into the borospherene cages in both exohedral and endohedral coordination patterns [3–16] including the newly reported actinide-doped endohedral metallo-borospherenes An@B400/+/- (An = U, Np, Pu, Am, Cm) [12] investigated through detailed bonding pattern analyses. Among these advancements, lanthanides (Ln)-doped endohedral borospherenes Ln@B400/+/- have emerged as a particularly interesting area, driven by the partially occupied 4f electronic configurations of lanthanide elements that render distinctive magnetic and catalytic properties to the systems. Doublet endohedral rare-earth-metal-doped Cs Sc@B40, C2v Y@B40, and C2v La@B40 were proposed at density-functional theory (DFT) level in 2015 [16]. Endohedral octet Eu-doped D2d Eu@B40 (8B2) and septet Gd-doped Cs Gd@B40 (7A") have also been predicted in DFT theory [14]. Joint experimental and theoretical investigation indicated that the perfect spherical trihedral metallo-borospherenes D3h Ln3B18- (Ln = La, Tb) feature three lanthanide centers coordinated in three adjacent equivalent η10-B10 decagons on the cage surface [17]. Core-shell-like La3&[B2@B17]- and La3&[B2@B18]- [18], Td La4[B@B4@B24]0/+/- [19] and Oh La6[La@B24]+/0 [20] have also been predicted in theory. Ln4f atomic orbitals (AOs) are traditionally thought to be contracted and inert. Recent evidence indicates they may play a significant role in the formation of covalent bonding interactions in lanthanide borides, as demonstrated in the experimentally observed planar C2v SmB6- which exhibits effective Sm-B covalent bonding interactions involving obvious participation of the Sm 4f AOs [21]. However, there have been no systematic investigations to date on the ground-state structures and coordination bonding patterns of Ln@B400/+/-. More critically, no quantitative investigations have been made so far to unveil the differences between the Ln 4f AOs and An 5f AOs in coordination bonding capacities in their endohedral metallo-borospherenes.

Keeping the inspirations above in mind, we focus in this work on the ground-state structures and coordination bonding patterns of a series of endohedral Ln@$B_{40}{}^{0/+}$ complexes. Comprehensive DFT investigations indicate that the ground-state doublet C_{2v} Ce@$B_{40}{}^{+}$ ($^2B_1$), triplet C_{2v} Ce@B_{40} ($^3A_2$), quartet C_{2v} Pr@B_{40} ($^4B_1$), quintet C_{2v} Nd@B_{40} ($^5A_1$), sextet C_2 Pm@B_{40} (^6A), septet C_{2v} Sm@B_{40} ($^7A_2$), octet D_{2d} Eu@B_{40} ($^8B_1$), and octet C_{2v} Gd@$B_{40}{}^{+}$ ($^8A_2$) possess monotonically decreasing coordination bonding energies in series. The percentage contribution of the Ln 5d-involved molecular orbitals in these species increase almost monotonically from 66 to 83%, while the Ln 4f-involved molecular orbitals making only minor contributions between 0.3%~12.0%. Detailed bonding analyses unveil the specific coordination bonding patterns of the Ln@$B_{40}{}^{0/+}$ series and quantitatively reveal the differences in coordination bonding capacities between Ln@$B_{40}{}^{0/+}$ and An@$B_{40}{}^{0/+/-}$.

Computational Methodology

The structures of endohedral Lanthanide-metal-doped Ln@$B_{40}{}^{0/+}$ (An = Ce, Pr, Nd, Pm, Sm, Eu, Gd) were fully optimized at both the hybrid DFT-PBE0 [22] and DFT-TPSSh [23] levels, with the 6-311 + G(d) [24] basis set used for B and the scalar-relativistic Stuttgart energy-consistent pseudopotential with the ECP28MWB_SEG [25] valence basis set employed for Ce-Eu and ECP28MWB_ANO [25–27] used for Gd. The DFT-PBE0 method has proven to be reliable in determining the ground-state structures of lanthanide-metal-doped metall-borospherenes $Ln_3B_{18}{}^{-}$ (Ln = La, Tb) in gas-phase photoelectron spectroscopy experiments. [17] Vibrational frequency and wavefunction stability analyses were performed at PBE0 level to make sure that all the low-lying isomers obtained are true minima of the systems without imaginary frequencies. All the PBE0 and TPSSh computations were performed using the Gaussian09 program [28]. Detailed Born-Oppenheimer molecular dynamic (BOMD) simulations were performed on Ce@$B_{40}{}^{+}$ (**1**), Ce@B_{40} (**2**), Pr@B_{40} (**3**), and Eu@B_{40} (**7**) at 500 K, Nd@B_{40} (**4**), Pm@B_{40} (**5**), and C_{2v} Sm@B_{40} (**6**) at 300 K, and Gd@$B_{40}{}^{+}$ (**8**) at 200 K. BOMD simulation was implemented employing the CP2K [29, 30] code with the GTH-PBE pseudopotentials for B and the TZVP-MOLOPTSR-GTH basis sets for lanthanide atoms, in the NVT ensemble using a Nosé-Hoover thermostat [31]. The infrared and Raman spectra of C_{2v} Ce@$B_{40}{}^{+}$ (**1**) and C_{2v} Ce@B_{40} (**2**) were simulated at PBE0/6-311 + G(d). The UV-vis absorption spectra of Eu@B_{40} (**7**) and Gd@$B_{40}{}^{+}$ (**8**) were simulated using the time-dependent DFT method (TD-DFT-PBE0) [32, 33]. Chemical bonding patterns were analyzed on the open-shell Ln@$B_{40}{}^{0/+}$ series employing both the adaptive natural density partitioning (AdNDP) [34, 35] and principal interaction spin orbital (PISO) [36–39] approaches. The PISO analyses were also carried out using the Gaussian 09 program with 6-31G* basis set used for B atom and ECP28MWB_SEG valence basis set employed for Ce-Eu and ECP28MWB_ANO used for Gd element. The VMD [40] program was used for the visualization of structures and molecular orbitals.

Results and Discussions

Structures and Stabilities

The optimized ground states of the doublet C_{2v} Ce@B_{40}^{+} (**1**, $^2B_1$), triplet C_{2v} Ce@B_{40} (**2**, $^3A_2$), quartet C_{2v} Pr@B_{40} (**3**, $^4B_1$), quintet C_{2v} Nd@B_{40} (**4**, $^5A_1$), sextet C_2 Pm@B_{40} (**5**, ^6A), septet C_{2v} Sm@B_{40} (**6**, $^7A_2$), octet D_{2d} Eu@B_{40} (**7**, $^8B_1$), and octet C_{2v} Gd@B_{40}^{+} (**8**, $^8A_2$) with slightly distorted or perfect D_{2d} structures are collectively shown in Fig. 1, with alternative low-lying isomers depicted in Fig. S1. Vibrational frequency analyses indicate that the ground states are all true minima on the potential energy surfaces of the systems with the lowest vibrational frequencies of 66.7, 72.1,75.6, 56.7, 81.2, 23.0, 36.0, and 73.9 cm^{-1}, respectively. The slightly off-centered ground-state doublet C_{2v} Ce@B_{40}^{+} (**1**, $^2B_1$) monocation with one unpaired 4f α-electron (n_α=1) lies 0.48 (0.52) eV and 2.44 (2.51) eV more stable than the quartet C_{2v} Ce@B_{40}^{+} ($^4A_2$) and sextet C_{2v} Ce@B_{40}^{+} ($^6B_2$) at PBE0 (TPSSh), respectively (Fig. S1). As expected, neutral C_{2v} Ce@B_{40} (**2**, $^3A_2$) adapts a triplet ground state with two unpaired α-electrons ($n_\alpha = 2$) which is 0.67 (0.21) and 0.57 (0.63) eV more stable than the singlet C_{2v} Ce@B_{40} ($^1A_1$) and quintet C_s Ce@B_{40} ($^5A'$) at PBE0 (TPSSh), respectively (Fig. S1). Detailed BOMD simulations in Fig. S2 indicate that Ce@B_{40}^{+} (**1**), Ce@B_{40} (**2**), Pr@B_{40} (**3**), and Eu@B_{40} (**7**) are all dynamically stable at 500 K, with the small calculated root-mean-square-deviations of RMSD = 0.09, 0.10, 0.11, 0.10 Å and maximum bond length deviations of MAXD = 0.31, 0.35, 0.40, 0.35 Å, respectively, while Nd@B_{40} (**4**), Pm@B_{40} (**5**), and Sm@B_{40} (**6**) are stable at 300 K, and Gd@B_{40}^{+} (**8**) is stable at 200 K, respectively. The optimized neutral Eu@B_{40} (**7**, $^8B_1$) appears to be the only species in the endohedral complex series which possesses a perfect D_{2d} geometry, in agreement with the prediction previously reported in Ref. [21]. It is also worth noticing that octet C_{2v} Gd@B_{40}^{+} (**8**, $^8A_2$) obtained at PBE0/ECP28MWB_ANO here (Fig. 1 and Fig. S1) possesses a higher symmetry than the previously predicted septet C_s Gd@B_{40} (^7A”) [21]. Additional calculations indicate that the same ground state of C_{2v} Gd@B_{40}^{+} (**8**, $^8A_2$) is obtained at PBE0 level with the basis set of ECP28MWB_SEG.

Bonding Pattern Analyses

The high stability of these endohedral metallo-borospherenes originates from their unique coordination bonding patterns. As a typical example with the highest spin multiplicity in the series, Fig. 2 shows the AdNDP and PISO bonding patterns of the octet D_{2d} Eu@B_{40} (**7**, $^8B_1$). As indicated in the AdNDP bonding pattern in Fig. 2(a), Eu@B_{40} (**7**) possesses 7 singly occupied 1c-1e bonds with the occupation numbers between ON = 0.97-1.00 on the Eu coordination center, 40 3c-2e delocalized σ-bonds with ON = 1.94–1.96 and 8 6c-2e delocalized σ-bonds with ON = 1.84 on the B_{40} ligand, 4 6c-2e, 4 7c-2e, and 4 8c-2e delocalized π-bonds between the Eu center and B_{40} ligand with ON = 1.68–1.80, and 1 40c-2e σ-bond on the B_{40} ligand with ON = 1.96, indicating that the 12 delocalized π-bonds which all involve the Eu coordination center dominate the coordination bonding interactions between the Eu core and the B_{40} ligand in the system.

Detailed PISO analyses on Eu@B_{40} (**7**) in Fig. 2(b) with the Eu coordination center and B_{40} ligand as interacting fragments help to provide a more accurate description of the coordination bonding pattern in the complex. It has seven unpaired α-PISO 4f orbitals (n_α = 7) with the PISO populations of 0.975, 0.975, 0.994, 0.997, 0.997, 0.998, and 0.998, respectively, as the singly occupied molecular

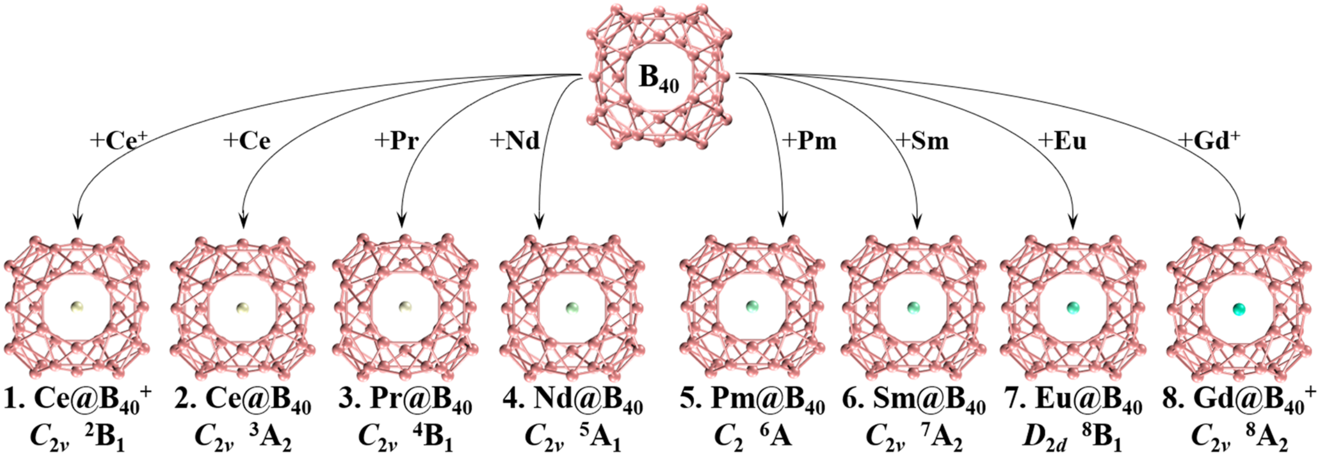

Fig. 1 Optimized ground-state structures of C_{2v} Ce@B_{40}^{+} (**1**, $^2B_1$), C_{2v} Ce@B_{40} (**2**, $^3A_2$), C_{2v} Pr@B_{40}^{+} (**3**, $^4B_1$), C_{2v} Nd@B_{40} (**4**, $^5A_1$), C_2 Pm@B_{40} (**5**, ^6A), C_{2v} Sm@B_{40} (**6**, $^7A_2$), C_{2v} Eu@B_{40} (**7**, $^8B_1$) and C_{2v} Gd@B_{40}^{+} (**8**, $^8A_2$) at PBE0 level with the numbers of unpaired α-electrons n_α = 1,2, 3,4, 5, 6, 7, and 7, respectively

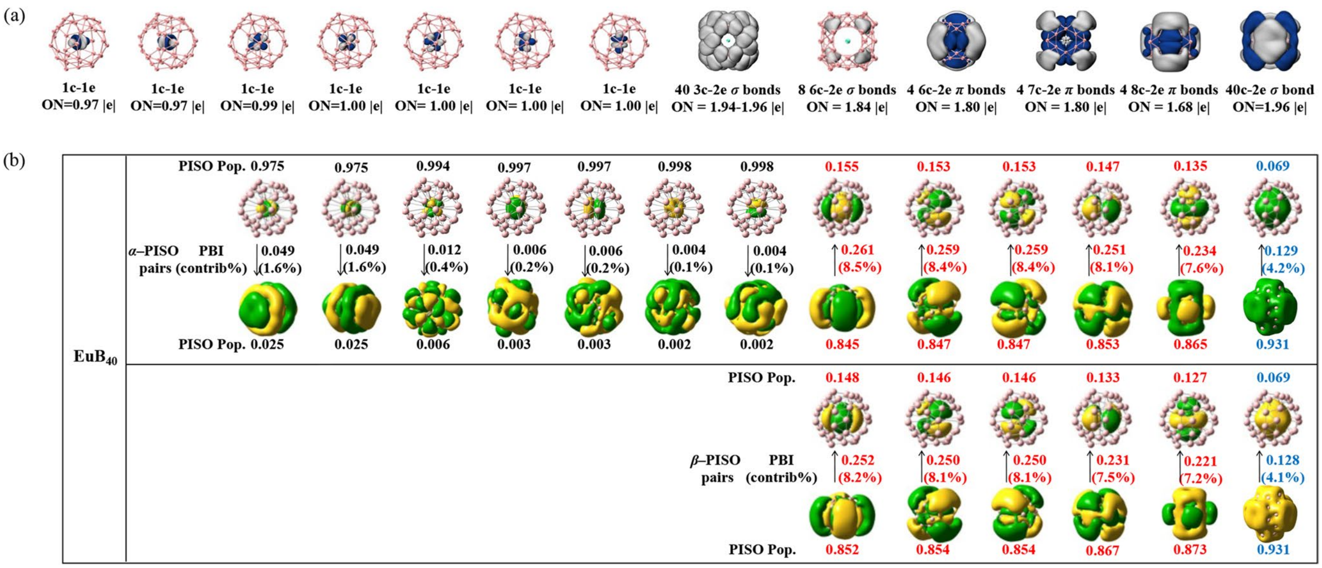

Fig. 2 (**a**) AdNDP bonding pattern of the octet D_{2d} Eu@B$_{40}$ (**7**, ^{8}B$_1$), with the occupation numbers (ON) indicated. (**b**) PISO bonding pattern of D_{2d} Eu@B$_{40}$ (**7**, ^{8}B$_1$) using the Eu coordination center and B$_{40}$ ligand as interacting fragments, with the corresponding occupation numbers (PISO Pop.), PISO-based bond indices (PBI), and percentage contributions (contrib/%) to the overall coordination interactions indicated

orbitals (α-SOMOs) of the complex, which have no the corresponding β-PISO counterparts to correlate with, while all the remaining α-PISO and β-PISO pairs in exact one-to-one corresponding relationships form doubly occupied molecular orbitals, rendering the system an octet ground state (^{8}B$_1$). The seven unpaired α-PISO 4f orbitals turn out to correspond to the seven 1c-1e bonds obtained by AdNDP analyses in Fig. 2(a), respectively. Their small PISO-based bond indices (PBI) between 0.004 and 0.049 indicate that the interactions between the seven unpaired α-PISO Eu 4f orbitals and the corresponding nearly empty α-molecular orbitals of the B$_{40}$ ligand with the small PISO populations between 0.002 and 0.025 make marginable contributions between 0.1% and 1.6% to the overall coordination energy of the complex. The next five α-PISO pairs and β-PISO pairs highlighted in red which have small but non-negligible PISO populations from Eu 5d AOs (between 0.135 and 0.155) are doubly occupied molecular orbitals which together contribute about 80.1% to the overall coordination energy in the complex, while the correlated α-PISO pair and β-PISO pair which possess the PISO population of 0.069 from Eu 6s atomic orbital in the last column highlighted in blue form another doubly occupied molecular orbital which contributes about 8.3% to the overall coordination energy of the system. Such a PISO bonding pattern clearly indicates that twelve π-coordination interactions between the B$_{40}$ ligand and Eu core mainly contain contributions from the Eu 5d-involved PISOs (80.1% in total), while the Eu 4f-involved PISOs (4.2% in total) and Eu 6s-involved PISO (8.3% in total) make only minor contributions to the overall coordination interactions in the system.

As shown in Fig. 3 and Fig. S3, Fig. S4, Fig. S5, and Fig. S6, similar AdNDP and PISO bonding patterns exist for doublet C_{2v} Ce@B$_{40}^+$ (**1**, ^{2}B$_1$), triplet C_{2v} Ce@B$_{40}$ (**2**, ^{3}A$_2$), quartet C_{2v} Pr@B$_{40}$ (**3**, ^{4}B$_1$), quintet C_{2v} Nd@B$_{40}$ (**4**, ^{5}A$_1$), sextet C_2 Pm@B$_{40}$ (**5**, ^{6}A), septet Sm@B$_{40}$ (**6**, ^{7}A$_2$), and octet C_{2v} Gd@B$_{40}^+$ (**8**, ^{8}A$_2$), which have the increasing number of unpaired α-electrons from n_α = 1, 2, 3, 4, 5, 6, to 7, respectively. Intriguingly, the first α-SOMO of the sextet Pm@B$_{40}$ (**5**, ^{6}A), which contributes 12.1% to the overall coordination interaction, turns out to be a typical α-bond with the comparable Pm 4f α-PISO population of 0.579 and B$_{40}$ α-PISO population of 0.421 and a PISO-based bond indices of PBI = 0.487. Such a singly occupied α-PISO pair with non-negligible contributions from both the Pm center and B$_{40}$ ligand corresponds to the 41c-1e covalent bond in the AdNDP bonding pattern shown at bottom in Fig. S5. Similar α-bond exists in quintet Nd@B$_{40}$ (**4**, ^{5}A$_1$) which contributes 5.4% to the overall coordination interaction with the Nd 4f α-PISO population of 0.138 and B$_{40}$ α-PISO population of 0.862 (Fig. 4). Thus, Ln 4f AOs make obvious contributions to the singly occupied α-bonds in both Nd@B$_{40}$ (**4**, ^{5}A$_1$) and Pm@B$_{40}$ (**5**, ^{6}A), analogous to the situation observed in SmB$_6^-$ which exhibits effective Sm-B covalent bonding interactions involving obvious participation of the Sm 4f Aos. [1] More interestingly, the first singly occupied α-SOMO of Ce@B$_{40}$ (**2**) which possesses the marginal Ce 4f α-PISO population of 0.947 corresponds to the 40c-1e

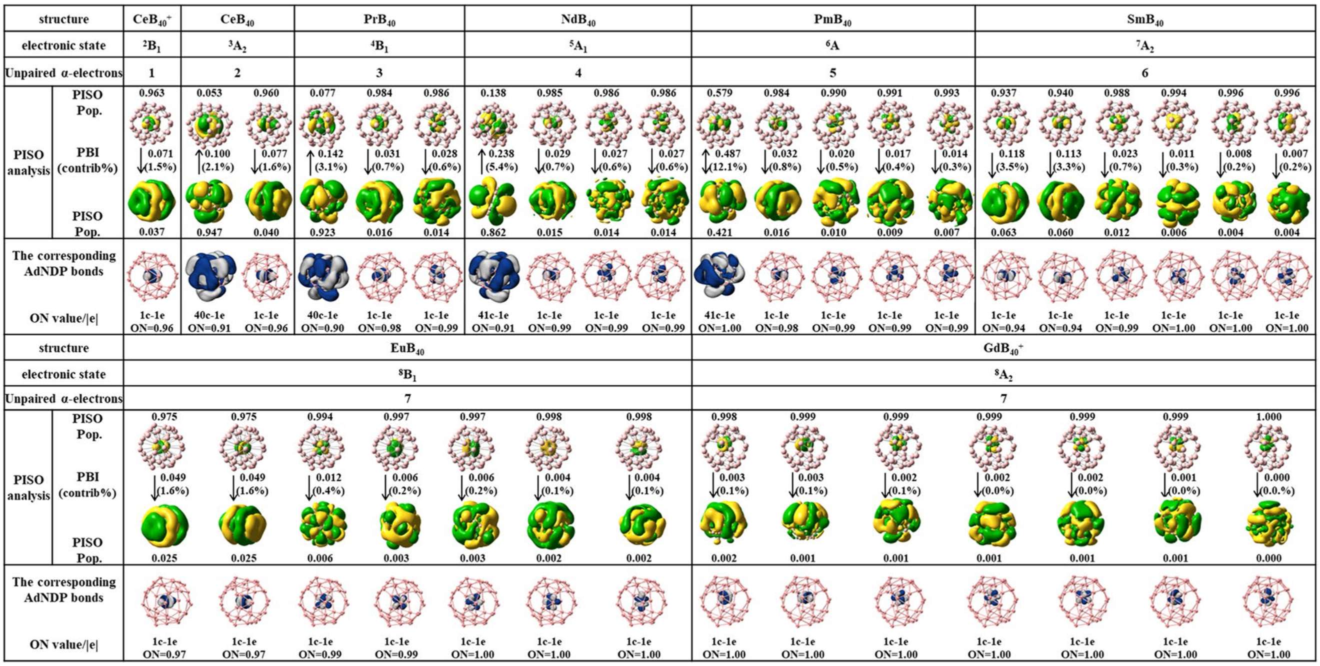

Fig. 3 Singly occupied PISO α-orbitals of Ce@B_{40}^+ (C_{2v}, $^2B_1$), Ce@B_{40} (C_{2v}, $^3A_2$), Pr@B_{40} (C_{2v}, $^4B_1$), Nd@B_{40} (C_2, $^5A_1$), Pm@B_{40} (C_2, ^6A), Sm@B_{40} (C_{2v}, $^7A_2$), Eu@B_{40} (D_{2d}, $^8B_1$), and Gd@B_{40}^+ (C_{2v}, $^8A_2$) with the α-spin populations (PISO Pop.) associated with the principal interacting spin orbitals, PISO-based bond indices (PBI), and their percentage contributions to the overall coordination interactions between the lanthanide coordination center and B_{40} ligand indicated. The corresponding singly occupied 1c-1e bonds in these species obtained by AdNDP analyses are shown at the bottom, with the occupation numbers (ON) indicated

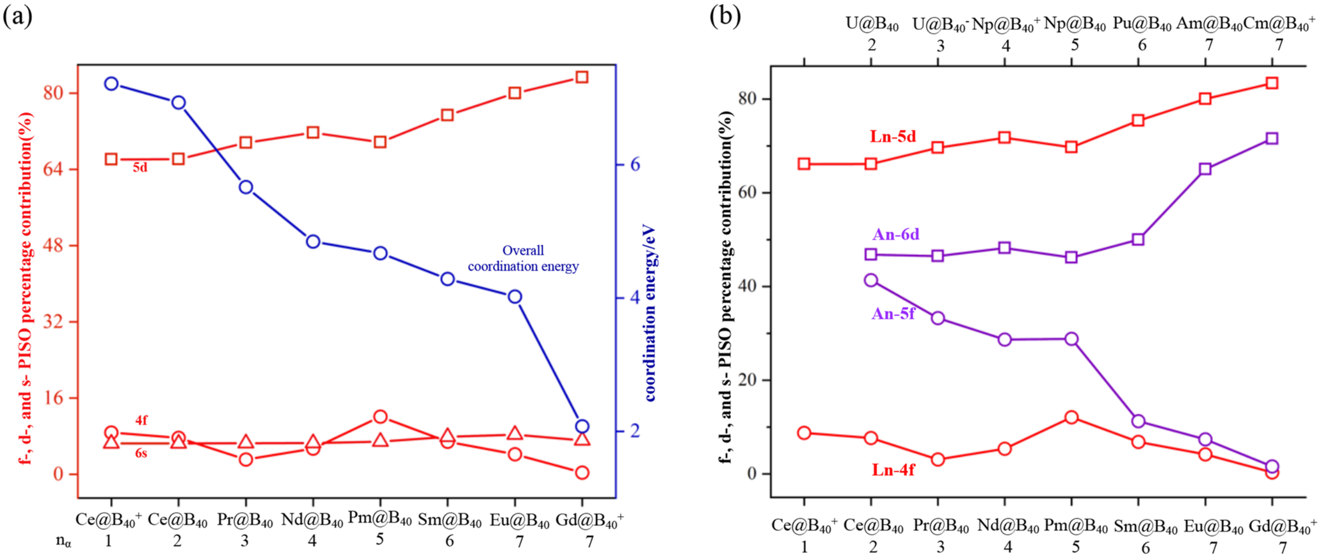

Fig. 4 (**a**) Variation of the calculated overall Ln–B_{40} coordination interaction energies (in eV) highlighted in blue and the corresponding PISO percentage contributions of 4f-, 5d-, and 6s-orbital-involved pair interactions highlighted in red in CeB_{40}^+ (C_{2v}, $^2B_1$), CeB_{40} (C_{2v}, $^3A_2$), PrB_{40} (C_{2v}, $^4B_1$), NdB_{40} (C_2, $^5A_1$), PmB_{40} (C_2, ^6A), SmB_{40} (C_{2v}, $^7A_2$), EuB_{40} (D_{2d}, $^8B_1$), and GdB_{40}^+ (C_{2v}, $^8A_2$) with the increasing numbers of unpaired α-electrons (n_α) in the systems at PBE0 level. (**b**) Comparison between the percentage contributions of 4f-involved and 5d-involved PISO pairs in Ln@$B_{40}^{0/+}$ (Ln = Ce, Pr, Nd, Pm, Sm, Eu, Gd) highlighted in red and 5f-involved and 6d-involved PISO pairs in An@$B_{40}^{0/+/-}$ (An = U, Np, Pu, Am, Cm) highlighted in purple with the increasing n_α in the systems

σ-bond on the B_{40} ligand with ON = 0.91, while the first singly occupied α-SOMO of quartet Pr@B_{40} (**3**) which has the minor Pr 4f α-PISO population of 0.077 and predominating B_{40} α-PISO population of 0.923 represents the 40c-1e σ-bond on the B_{40} ligand with ON = 0.90. Neutral Ce@B_{40} (**2**) and Pr@B_{40} (**3**) can thus be viewed as charge-transfer complexes Ce^+@B_{40}^- (**2**) and Pr^+@B_{40}^- (**3**) with an α-electron almost completely transferred from the Ln lanthanide center to B_{40} ligand, with the corresponding electrostatic interactions contributing 2.1% and 3.1% to the overall coordination energies of the corresponding systems, respectively. The results obtained above suggest that, relative to the weak ionic interactions of $Ce^{+}@B_{40}^{-}$ (**2**) and $Pr^{+}@B_{40}^{-}$ (**3**) in PISO approach, covalent interactions predominate the coordination interactions in these lanthanide-doped metallo-borospherene complexes.

Percentage Contributions of Ln 4f-, 5d-, and 6s-involved PISO Pairs To the Total Coordination Interactions

In order to compare the percentage contributions of Ln 4f-, 5d-, and 6s-involved PISO pairs to the overall Ln–B_{40} coordination interaction energies, we categorized the orbital types of Ln atoms involved in the PISO bonding patterns by their orbital shapes and considered the contributions of the corresponding PISO pairs separately. As illustrated in Fig. 4(a), as the number of unpaired α-electrons with parallel spins increases from n_{α} = 1, 2, 3, 4, 5, 6, 7 and 7 in the $Ce@B_{40}^{+}$ (**1**), $Ce@B_{40}$ (**2**), $Pr@B_{40}$ (**3**), $Nd@B_{40}$ (**4**), $Pm@B_{40}$ (**5**), $Sm@B_{40}$ (**6**), $Eu@B_{40}$ (**7**), and $Gd@B_{40}^{+}$ (**8**) series, the calculated overall Ln-B_{40} coordination interaction energies decrease monotonically from E_{c} = 7.22, 6.93, 5.67, 4.85, 4.67, 4.29, 4.02, to 2.07 eV, respectively. In percentage contributions, the dominating contributions of the Ln 5d-involved PISO pairs to the overall E_{c} increase almost monotonically from 66.1%, 66.2%, 69.9%, 71.8%, 69.7%, 75.4%, 80.0–83.4%, while the corresponding minor contributions of the Ln 4f-involved PISO pairs vary from 8.8%, 7.7%, 3.1%, 5.4%, 12.1%, 6.8%, 4.2%, to 0.3% and that of Ln 6s-involved PISO pairs remain basically unchanged in the narrow range from 6.5%, 6.5%, 6.5%, 6.6%, 6.9%, 7.9%, 8.3%, to 7.1%.

As shown in Fig. 4(b), PISO analyses also provide a quantitative way to identify the difference in coordination bonding patterns between lanthanide-doped borospherenes highlighted in red and actinide-doped endohedral borospherenes highlighted in purple. [22] With the numbers of the unpaired α-electrons increasing from n_{α} = 1 to 7, the contributions of Ln 5d-involved PISO pairs in $Ln@B_{40}^{+/0}$ increase monotonically from 66 to 83% and the contributions of An 6d-involved PISO pairs $An@B_{40}^{+/0/-}$ increase monotonically from 47–72% [22], while the contributions of Ln 4f-involved PISO pairs vary between 0.3 and 12.0% and the contributions of the An 5f-involved PISO pairs decrease monotonically from 41% to 1%. In average, the dominating Ln 5d-invloved PISO pairs contribute about 72.8% to the overall coordination bonding energies in $Ln@B_{40}^{+/0}$, 19.3% higher than that (53.5%) of the An 6d-involved PISO pairs in $An@B_{40}^{+/0/-}$ [22], while the minor 4f-involved PISO pairs in $Ln@B_{40}$ contribute about 6.1% to the overall E_{c}, 15.7% lower than that (21.8%) of the 5f-invloved PISOs in $An@B_{40}^{+/0/-}$. These observations agree with the fundamental electronic structure differences between lanthanides and actinides, where the Ln 4f orbitals in lanthanides exhibit less spatial extension and weaker bonding capability than the An 5f orbitals in actinides, while the Ln 5 d orbitals in the former exhibit greater spatial extension and stronger bonding capability than the An 6 d orbitals in actinides. Both Ln 6s-involved and An 7s-involved PISO pairs appear to make minor contributions to the overall coordination interaction energies in their boride complexes.

Simulated IR, Raman and UV-Vis Spectra

The IR and Raman spectra of C_{2v} $Ce@B_{40}^{+}$ (**1**, $^{2}B_{1}$) and C_{2v} GdB_{40}^{+} (**8**, $^{8}A_{2}$) are depicted in Fig. 5(a) at PBE0 level to facilitate their future experimental characterizations. $Ce@B_{40}^{+}$ (**1**) exhibits four distinct IR absorption peaks at 725 (b_{2}), 808 (a_{1}), 1119 (b_{2}), and 1284 (b_{2}) cm^{-1}, corresponding to the tangential vibrational modes b_{2}, a_{1}, b_{2}, and b_{2} of the B_{40} boron skeleton, respectively., respectively [23] In the Raman spectrum, characteristic vibrational modes are identified at 247 (b_{1}), 277 (a_{2}), 454 (a_{1}), and 635 (a_{1}) cm^{-1}. Similar IR and Raman spectra features are obtained for $Gd@B_{40}^{+}$ (**8**). Notably, $Ce@B_{40}^{+}$ (**1**) and $Gd@B_{40}^{+}$ (**8**) exhibit characteristic radial breathing modes (RBMs) at 454 cm^{-1} (a_{1}) and 463 cm^{-1} (a_{1}), respectively, which are slightly blue-shifted compared to the RBM of the empty D_{2d} B_{40} borospherene (428 cm^{-1} (a_{1})) at the same theoretical level. The UV-Vis spectra of neutral C_{2v} $Ce@B_{40}$ (**2**) and D_{2d} EuB_{40} (**7**) are also computationally simulated in Fig. 5(b) using TD-DFT-PBE0 approach with 200 excited states included. For $Ce@B_{40}$ (**2**), the main adsorption peaks occur at 344 ($^{3}A_{1}$), 388 ($^{3}A_{1}$), 404 ($^{3}A_{1}$), and 559 ($^{3}B_{2}$) nm, while for $Eu@B_{40}$ (**7**), the primary absorption peaks are predicted at 366 ($^{8}B_{2}$), 399 (^{8}E), 448 ($^{8}B_{2}$), and 659 (^{8}E) nm.

Conclusion

We have predicted in this work the ground-state structures of doublet $Ce@B_{40}^{+}$ (**1**), triplet $Ce@B_{40}$ (**2**), quartet $Pr@B_{40}$ (**3**), quintet $Nd@B_{40}$ (**4**), sextet $Pm@B_{40}$ (**5**), septet $Sm@B_{40}$ (**6**), octet $Eu@B_{40}$ (**7**), and octet $Gd@B_{40}^{+}$ (**8**) at both PBE0 and TPSSh levels, revealed their coordination bonding patterns using both the PISO and AdNDP approaches, and calculated the percentage contributions of Ln 4f-, 5d-, and 6s-involved PISO pairs to the overall coordination interaction energies at PBE0, deciphering

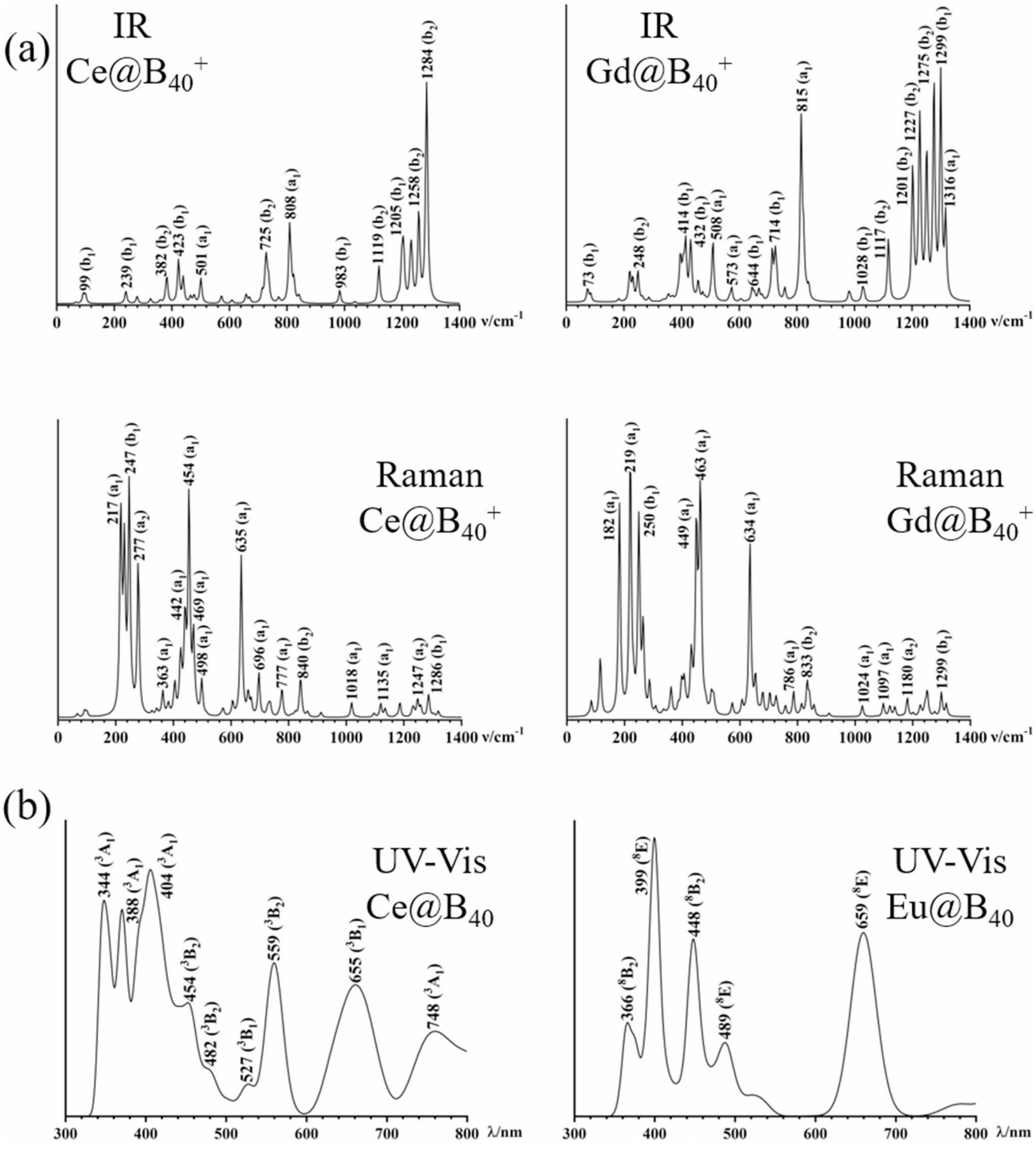

Fig. 5 Simulated (**a**) IR and Raman spectra of C_{2v} Ce@B$_{40}^+$ (**1**, ^{2}B$_1$) and C_{2v} Gd@B$_{40}^+$ (**8**, ^{8}A$_2$) and (**b**) UV-Vis spectra of C_{2v} Ce@B$_{40}$ (**2**, ^{3}A$_2$) and D_{2d} Eu@B$_{40}$ (**7**, ^{8}B$_1$) at PBE0 level

the coordination bonding nature of these lanthanide-doped endohedral metallo-borospherenes both qualitatively and quantitatively. In average, the minor Ln 4f-involved PISOs in Ln@B$_{40}$ contribute about 15.7% less than that of the An 5f-invloved PISOs in An@B$_{40}^{+/0/-}$, while the dominating Ln 5d-invloved PISOs in Ln@B$_{40}$ contribute 19.3% more than that of the An 6d-involved PISOs in An@B$_{40}^{+/0/-}$. Ln 4f AOs are found to make obvious contributions to the singly occupied α-bonds in both Nd@B$_{40}$ (**4**) and Pm@B$_{40}$ (**5**) which belong to covalent bonding interactions between the

Ln center and B_{40} ligand. Such high-spin lanthanide-doped endohedral metallo-borospheres could be realized in future experiments to form various nanoclusters and nanocrystals which may have wide potential applications in both chemistry and materials science.

Supplementary Information The online version contains supplementary material available at https://doi.org/10.1007/s10876-025-02908-w.

Author Contributions S-D Li designed the project and finalized the manuscript and X-N Zhao, T Zhang and X-Q Lu performed the calculations. All the authors participated in the discussion and preparation of the manuscript.

Funding The work was supported by the National Natural Science Foundation of China (22373061 and 21973057 to S.-D. Li).

Data Availability No datasets were generated or analysed during the current study.

Declarations

Competing Interests The authors declare no competing interests.

References

1. Zhai HJ, Zhao YF, Li WL et al (2014) Observation of an all-boron fullerene. Nat Chem 6:727–731. https://doi.org/10.1038/nchem.1999
2. Chen Q, Li WL, Zhao YF et al (2015) Experimental and theoretical evidence of an axially chiral borospherene. ACS Nano 9:754–760. https://doi.org/10.1021/nn506262c
3. Bai H, Chen Q, Zhai HJ, Li SD (2015) Endohedral and exohedral metalloborospherenes: M@B (M = Ca, Sr) and M&B (M = Be, Mg). Angew Chem Int Ed 54:941–945. https://doi.org/10.1002/anie.201408738
4. Fa W, Chen S, Pande S, Zeng XC (2015) Stability of Metal-Encapsulating Boron Fullerene B. J Phys Chem A 119:11208–11214. https://doi.org/10.1021/acs.jpca.5b07173
5. Bai H, Bai B, Zhang L et al (2016) Lithium-Decorated Borospherene B40: A Promising Hydrogen Storage Medium. Sci Rep 6:1–10. https://doi.org/10.1038/srep35518
6. An Y, Zhang M, Wu D, et al (2016) Electronic transport properties of the first all-boron fullerene B40 and its metallofullerene Sr@B40. Phys Chem Chem Phys 18:12024–12028. https://doi.org/10.1039/c6cp01096b
7. Li HR, Tian XX, Luo XM, et al (2017) Heteroborospherene clusters Ni €B (n = 1–4) and heteroborophene monolayers Ni € B with planar heptacoordinate transition-metal centers in η -B heptagons. Sci Rep 7:1–7. https://doi.org/10.1038/s41598-017-06039-9
8. Jin P, Yang L, Liu C et al (2017) Computational prediction of the endohedral metalloborofullerenes Ti @B (n = 1, 2). Theor Chem Acc 136:56–67. https://doi.org/10.1007/s00214-017-2087-x
9. Yu T, Gao Y, Xu D, Wang Z (2018) Actinide endohedral boron clusters: A closed-shell electronic structure of U@B . Nano Res 11:354–359. https://doi.org/10.1007/s12274-017-1637-9
10. Keyhanian M, Farmanzadeh D (2019) The role of Mn and Fe transition metal atoms mediation on the aniline adsorption by B40 fullerene: A computational investigation. J Mol Liq 294:111638. https://doi.org/10.1016/j.molliq.2019.111638
11. Li Y, Wang Y, Zhou Z et al (2024) Insights into ThB40: Stability, Electronic Structure, and Interaction. Molecules 29:1222–1232. https://doi.org/10.3390/molecules29061222
12. Zhao XN, Wei ZH, Li SD (2024) Investigation on the Coordination Bonding Nature of Actinide-Doped Endohedral Borospherenes An@B400/+/– (An = U, Np, Pu, Am, Cm). Molecules 29:5879–5888. https://doi.org/10.3390/molecules29245879
13. Li P, Wei J, Wei H, et al (2022) A Systemic Insight into Exohedral Actinides and Endohedral Borospherenes: An&B_m and An@B_n (An = U, Np, Pu; m = 28, 32, 34, 36, 38, 40; n = 36, 38, 40). Molecules 27:6047–6057. https://doi.org/10.3390/molecules27186047
14. Xi C, Yang L, Liu C, et al (2018) Lanthanide metals in the boron cages: Computational prediction of M@Bn (M = Eu, Gd; n = 38, 40). Int J Quantum Chem 118:25576–25586. https://doi.org/10.1002/qua.25576
15. Li SX, Zhang ZP, Long ZW, Qin SJ (2017) Structures, stabilities and spectral properties of metalloborospheres MB400/- (M = Cu, Ag, and Au). RSC Adv 7:38526–38537. https://doi.org/10.1039/c7ra05932a
16. Jin P, Hou Q, Tang C, Chen Z (2015) Computational investigation on the endohedral borofullerenes M@B40 (M = Sc, Y, La). Theor Chem Acc 134:13. https://doi.org/10.1007/s00214-014-1612-4
17. Chen TT, Li WL, Chen WJ, et al (2020) Spherical trihedral metallo-borospherenes. Nat Commun 11:2766–2773. https://doi.org/10.1038/s41467-020-16532-x
18. Zhao XY, Yan M, Wei Z, Li SD (2020) Donor-acceptor duality of the transition-metal-like B2 core in core-shell-like metallo-borospherenes La3&[B2@B17]-and La3&[B2@B18]-. RSC Adv 10:34225–34230.
19. Lu X-Q, Gao C-Y, Wei Z, Li S-D (2021) Cage-like La4B24 and Core-Shell La4B290/+/− : perfect spherically aromatic tetrahedral metallo-borospherenes. J Mol Model 27:130–136. https://doi.org/10.1007/s00894-021-04739-8
20. Lu XQ, AoMZ Tian XX et al (2020) Perfect cubic La-doped boron clusters La_6&$[La@B_{24}]^{+/0}$as the embryos of low-dimensional lanthanide boride nanomaterials. RSC Adv 10:12469–12474. https://doi.org/10.1039/d0ra01616k
21. Robinson PJ, Zhang X, McQueen T, et al (2017) SmB_6^- Cluster Anion: Covalency Involving f Orbitals. J Phys Chem A 121:1849–1854. https://doi.org/10.1021/acs.jpca.7b00247
22. Adamo C, Barone V (1999) Toward reliable density functional methods without adjustable parameters: The PBE0 model. J Chem Phys 110:6158–6170. https://doi.org/10.1063/1.478522
23. Staroverov VN, Scuseria GE, Tao J, Perdew JP (2003) Comparative assessment of a new nonempirical density functional: Molecules and hydrogen-bonded complexes. J Chem Phys 119:12129–12137. https://doi.org/10.1063/1.1626543
24. Krishnan R, Binkley JS, Seeger R, Pople JA (1980) Self-consistent molecular orbital methods. XX. A basis set for correlated wave functions. J Chem Phys 72:650–654. https://doi.org/10.1063/1.438955
25. Dolg M, Stoll H, Preuss H (1989) Energy-adjusted ab initio pseudopotentials for the rare earth elements. J Chem Phys 90:1730–1734. https://doi.org/10.1063/1.456066
26. Cao X, Dolg M (2001) Valence basis sets for relativistic energy-consistent small-core lanthanide pseudopotentials. J Chem Phys 115:7348–7355. https://doi.org/10.1063/1.1406535
27. Cao X, Dolg M (2004) Segmented contraction scheme for small-core actinide pseudopotential basis sets. J Mol Struct: THEOCHEM 673:203–209. https://doi.org/10.1016/j.theochem.2003.12.015
28. Frisch MJ, Trucks GW, Schlegel HB et al (2013) Gaussian 09, Revision D.01, GaussianInc., Wallingford CT

29. Vandevondele J, Krack M, Mohamed F, et al (2005) Quickstep: Fast and accurate density functional calculations using a mixed Gaussian and plane waves approach. Comput Phys Commun 167:103–128. https://doi.org/10.1016/j.cpc.2004.12.014
30. Kühne TD, Iannuzzi M, Del Ben M et al (2020) CP2K: An electronic structure and molecular dynamics software package -Quickstep: Efficient and accurate electronic structure calculations. J Chem Phys 152:194103–194149
31. Nosé S (1984) A unified formulation of the constant temperature molecular dynamics methods. J Chem Phys 81:511–519.https://doi.org/10.1063/1.447334
32. Casida ME, Jamorski C, Casida KC, Salahub DR (1998) Molecular excitation energies to high-lying bound states from time-dependent density-functional response theory: Characterization and correction of the time-dependent local density approximation ionization threshold. J Chem Phys 108:4439–4449. https://doi.org/10.1063/1.475855
33. Bauernschmitt R, Ahlrichs R (1996) Treatment of electronic excitations within the adiabatic approximation of time dependent density functional theory. Chem Phys Lett 256:454–464. https://doi.org/10.1016/0009-2614(96)00440-X
34. Zubarev DY, Boldyrev AI (2008) Developing paradigms of chemical bonding: Adaptive natural density partitioning. Phys Chem Chem Phys 10:5207–5217. https://doi.org/10.1039/b804083d
35. Tkachenko N V., Boldyrev AI (2019) Chemical bonding analysis of excited states using the adaptive natural density partitioning method. Phys Chem Chem Phys 21:9590–9596. https://doi.org/10.1039/c9cp00379g
36. Zhang JX, Sheong FK, Lin Z (2018) Unravelling Chemical Interactions with Principal Interacting Orbital Analysis. Chem - Eur J 24:9639–9650. https://doi.org/10.1002/chem.201801220
37. Sheong FK, Zhang JX, Lin Z (2020) Principal interacting spin orbital: Understanding the fragment interactions in open-shell systems. Phys Chem Chem Phys 22:10076–10086. https://doi.org/10.1039/d0cp00127a
38. Sheong FK, Zhang JX, Lin Z (2020) Modular bonding picture for aromatic borometallic molecular wheels. Theor Chem Acc 139: 14. https://doi.org/10.1007/s00214-019-2536-9
39. Zhang J-X, Sheong FK, Lin Z (2020) Principal interacting orbital: A chemically intuitive method for deciphering bonding interaction. WIREs Comput Mol Sci 10:e1469. https://doi.org/10.1002/wcms.1469
40. Humphrey W, Dalke A, Schulten K (1996) VMD: Visual molecular dynamics. J Mol Graph 14:33–38. https://doi.org/10.1016/0263-7855(96)00018-5

Authors and Affiliations

Xiao-Ni Zhao[1] · Ting Zhang[1] · Xiao-Qin Lu[2] · Si-Dian Li[1]

✉ Si-Dian Li
lisidian@sxu.edu.cn

[1] Nanocluster Laboratory, Institute of Molecular Science, Shanxi University, Taiyuan, Shanxi 030006, China

[2] Shanxi Center for Testing of Functional Agro-Products, Shanxi Agricultural University, Taiyuan 030031Shanxi, China